Materials Chemistry and Physics 367 (2026) 132979

Contents lists available at ScienceDirect

Materials Chemistry and Physics

journal homepage: www.elsevier.com/locate/matchemphys

Structural and morphological evolution of $MoSe_2$ thin films as interlayers in phase-change heterostructures

Agnese Foglietti [a,b], Sara De Simone [a,*], Adriano Diaz Fattorini [c], Sabrina Calvi [a,c], Valentina Mussi [a], Christian Petrucci [a,c], Fabrizio Arciprete [a,c], Massimo Longo [b,**], Raffaella Calarco [a]

[a] Institute for Microelectronics and Microsystems (IMM), Consiglio Nazionale Delle Ricerche (CNR), Via Del Fosso Del Cavaliere 100, 00133, Rome, Italy
[b] Department of Chemical Science and Technologies, University of "Tor Vergata", Via Della Ricerca Scientifica 1, 00133, Rome, Italy
[c] Department of Physics University of "Tor Vergata", Via Della Ricerca Scientifica 1, 00133, Rome, Italy

HIGHLIGHTS

- Optimization of MoSe2 growth by RF-sputtering at room temperature.
- XRD/Raman study: 2H phase identification and 250 °C onset temperature.
- AFM analysis: increased density and c-axis oriented grain growth.
- Electrical behavior: increased resistivity post-annealing due to lamellar structure.
- MoSe2 stability as a confinement layer in GST225-based heterostructures.

ARTICLE INFO

Keywords:
PCM
$MoSe_2$
GST
Sputtering
Crystallization

ABSTRACT

Molybdenum diselenide ($MoSe_2$) is attracting interest as interlayer material in phase-change memories, where it can limit elemental diffusion and stabilize device operation. Here, we investigate thin $MoSe_2$ films deposited by RF sputtering at room temperature and analyze their structural and electrical response upon thermal treatment. As-grown films crystallize into a structure compatible with the 2H phase above 250 °C, with the appearance of diffraction peaks and vibrational modes typical of $MoSe_2$. This transition is accompanied by a densification of the films and a reorganization of the surface into compact grains, as revealed by X-ray reflectivity and microscopy. Raman spectra show the coexistence of well-defined phonon modes and disorder-related features, while electrical measurements show anomalous behavior after annealing at 300 °C, which may be attributed to morphology-related effects. Importantly, $MoSe_2$ maintains its stoichiometry after deposition and annealing, demonstrating chemical stability. When integrated into GST225/$MoSe_2$ heterostructures, the material preserves its integrity and withstands annealing up to 300 °C, confirming its compatibility with phase-change layers to be switched back and forth between their as-grown and crystalline states. These findings support the use of sputtered $MoSe_2$ as a robust interlayer in next-generation phase change memory devices.

1. Introduction

Phase-change memory (PCM) technology, which relies on chalcogenide materials such as $Ge_2Sb_2Te_5$ (GST225), has emerged as a promising candidate for next-generation non-volatile memory due to its fast switching speeds and scalability [1]. However, PCM encounters significant challenges, including resistance drift, high RESET currents, and limited thermal stability [2].

Among the different phase-change materials, GST225 is widely regarded as a benchmark for PCM technology because it offers a favorable trade-off between switching speed, electrical contrast, crystallization temperature, and long-term data retention. Other materials,

* Corresponding author.
** Corresponding author.
E-mail addresses: sara.desimone@cnr.it (S. De Simone), massimo.longo@uniroma2.it (M. Longo).

https://doi.org/10.1016/j.matchemphys.2026.132979
Received 15 May 2026; Received in revised form 21 July 2026; Accepted 31 July 2026
Available online 1 August 2026

such as Sb_2Te_3, are frequently employed in fundamental studies of phase-change heterostructures, however the relatively low crystallization temperature of Sb_2Te_3, typically in the range of 100–130 °C, results in poor thermal stability and limited data retention, making pure Sb_2Te_3 less suitable for practical non-volatile memory applications, unless it is combined with materials exhibiting higher crystallization temperatures. In contrast, GST225 typically exhibits a higher crystallization temperature of approximately 160 °C, while maintaining fast switching kinetics and excellent long-term data retention.

To address the limitations of conventional PCM materials, researchers have explored the use of heterostructures consisting of alternating layers of different phase-change materials [3] or phase-change layers separated by a confinement material, typically a transition metal dichalcogenide (TMD) [4]. For example, Ding et al. [5] demonstrated that phase-change heterostructures can suppress both electrical noise and resistance drift, resulting in more stable memory operation. Similarly, Bertelli et al. [3] reported that Ge–Sb–Te heterostructures exhibit higher crystallization-onset temperatures and reduced Ge segregation, thereby improving thermal stability.

Despite these advancements, heterostructures composed solely of phase-change materials do not fully overcome PCM's inherent limitations. Issues such as elemental diffusion and structural instability persist [6], necessitating alternative approaches. In particular, because adjacent phase-change layers undergo substantial atomic rearrangement during crystallization and melting, intermixing and compositional changes can still occur across their interfaces.

One promising pathway involves the integration of two-dimensional transition metal dichalcogenides into PCM devices [7]. These materials can be introduced as thin layers between active phase-change layers, serving as confinement barriers against long-range atomic diffusion. This may help reduce the compositional fluctuations caused by the volume and density changes occurring during the phase transition [8].

However, not all TMDs are equally effective as confinement materials. Their suitability depends on several factors, including chemical and thermal stability, electrical resistivity, thermal transport properties, defect concentration, and resistance to interdiffusion. For instance, $TiTe_2$ has been found to diffuse excessively into adjacent layers [4], compromising the integrity of the heterostructure. Conversely, a highly resistive TMD layer may hinder electrical transport, whereas an unstable layer may degrade during the thermal treatments or switching cycles required for PCM operation. This highlights the importance of selecting and evaluating confinement materials according to the specific requirements of the intended heterostructure.

In this context, $MoSe_2$ was selected because it combines structural, thermal, electronic, and technological characteristics that make it an interesting candidate for GST225-based heterostructures. $MoSe_2$ has been reported to exhibit good thermal stability and tunable electronic properties [9]. Nevertheless, the thermal behavior of sputtered $MoSe_2$ films cannot be directly inferred from results obtained on exfoliated or highly crystalline few-layer materials. In sputtered polycrystalline films, heat transport and structural stability may be strongly affected by grain boundaries, defects, film orientation, thickness and deviations from stoichiometry. Therefore, the suitability of sputtered $MoSe_2$ as a potential confinement layer should be experimentally assessed under thermal conditions representative of PCM processing.

While materials such as MoS_2, WS_2, or $MoTe_2$ have been widely investigated for micro- and optoelectronic applications, their integration in GST-based heterostructures for phase change devices has been studied and reported to a much lesser extent.

In particular, limited information is available on the structural evolution and thermal compatibility of sputtered $MoSe_2$ combined with GST225 during the phase transition. Investigating these aspects is essential because a confinement layer must maintain its structural and chemical integrity during the crystallization of the adjacent phase-change material.

In this work, we studied the radio-frequency (RF) sputtering deposition at room temperature (RT) and the subsequent crystallization of single $MoSe_2$ films on Si(100). While various growth strategies have been developed for transition metal dichalcogenides, including chemical vapor deposition (CVD), molecular beam epitaxy (MBE), and thermally assisted selenization, RF sputtering was selected as a scalable and industry-compatible technique [10–12]. In addition, room-temperature sputtering limits the thermal exposure of the underlying materials and is therefore particularly suitable for the fabrication of GST225-based multilayers.

At the same time, room-temperature-sputtered $MoSe_2$ films may initially exhibit structural disorder, small grain size, selenium deficiency, or deviations from the ideal stoichiometry. Subsequent annealing may improve their crystallinity but may also induce selenium loss, morphological changes, interdiffusion, or reactions with adjacent layers. A detailed investigation of their crystallization process and thermal behaviour is therefore required before their integration into functional PCM devices.

In this framework, the present work was conceived to investigate the structural evolution and thermal compatibility of sputtered $MoSe_2$ under conditions relevant to PCM technology, therefore GST225 was selected as the active phase-change material, and $MoSe_2$ films were inserted between GST225 layers and evaluated as potential confinement layers in a technologically relevant multilayered structure.

During annealing, the structural properties of the samples were studied by means of temperature-dependent X-ray diffraction measurements in grazing-incidence geometry, while atomic force microscopy was used to investigate the surface morphology. The vibrational properties were investigated by means of Raman spectroscopy. Electrical measurements in a four-point-probe configuration using a linear resistance-to-length method were performed to determine the film resistivity. X-ray fluorescence measurements were carried out to assess the elemental composition of both the $MoSe_2$ sputtering target and the deposited thin films. Two complementary annealing experiments were performed to investigate the crystallization behavior of $MoSe_2$ and its structural stability when integrated with GST225. It has to be emphasized that this work focuses on the materials aspects of $MoSe_2$ and $MoSe_2$/GST225 heterostructures rather than on device-level performance. For this reason, the goal is to assess whether sputtered $MoSe_2$ maintains its structural integrity during annealing and remains compatible with GST225 under processing conditions relevant to phase-change memories. Device fabrication and performance evaluation are beyond the scope of this study and will be addressed in future work.

2. Results and discussion

Fig. 1a shows the GID X-ray (ω - 2θ) scans of a single 20 nm thick film of $MoSe_2$ capped with a 20 nm thick Si_3N_4 film during annealing in N_2 atmosphere (within the temperature range $T = 30 \div 350$ °C). The GID measurement at 30 °C shows that the as-grown film is not crystalline, as no diffraction peak expected for $MoSe_2$ is visible. However, we observed a weak feature at 44°, which can be attributed to the Inconel clips used to secure the sample to the heating stage and a sharp peak at 51.3° that originates from the (−311) reflection of the silicon substrate. The sample crystallization sets in with the temperature increasing from 250 °C to 300 °C. The spectrum at 300 °C exhibits the main peak of $MoSe_2$, corresponding to the (0002) reflection located at 13.2°, compatible with previous literature reports [13]. This annealing experiment was carried out by increasing the temperature in steps of 50 °C and maintaining the temperature constant for 30 min, during the time needed for measuring the spectra.

When the highest temperature of 350 °C was reached, the sample was cooled down to RT and the spectrum was collected during a 2-h measurement. By proceeding in this way, we only detected the $MoSe_2$ (0002) peak, which indicated that the sample was crystallized with a strong preferential orientation along the (000ℓ) orientation. Such a finding suggests that our $MoSe_2$ crystallizes in a structure compatible

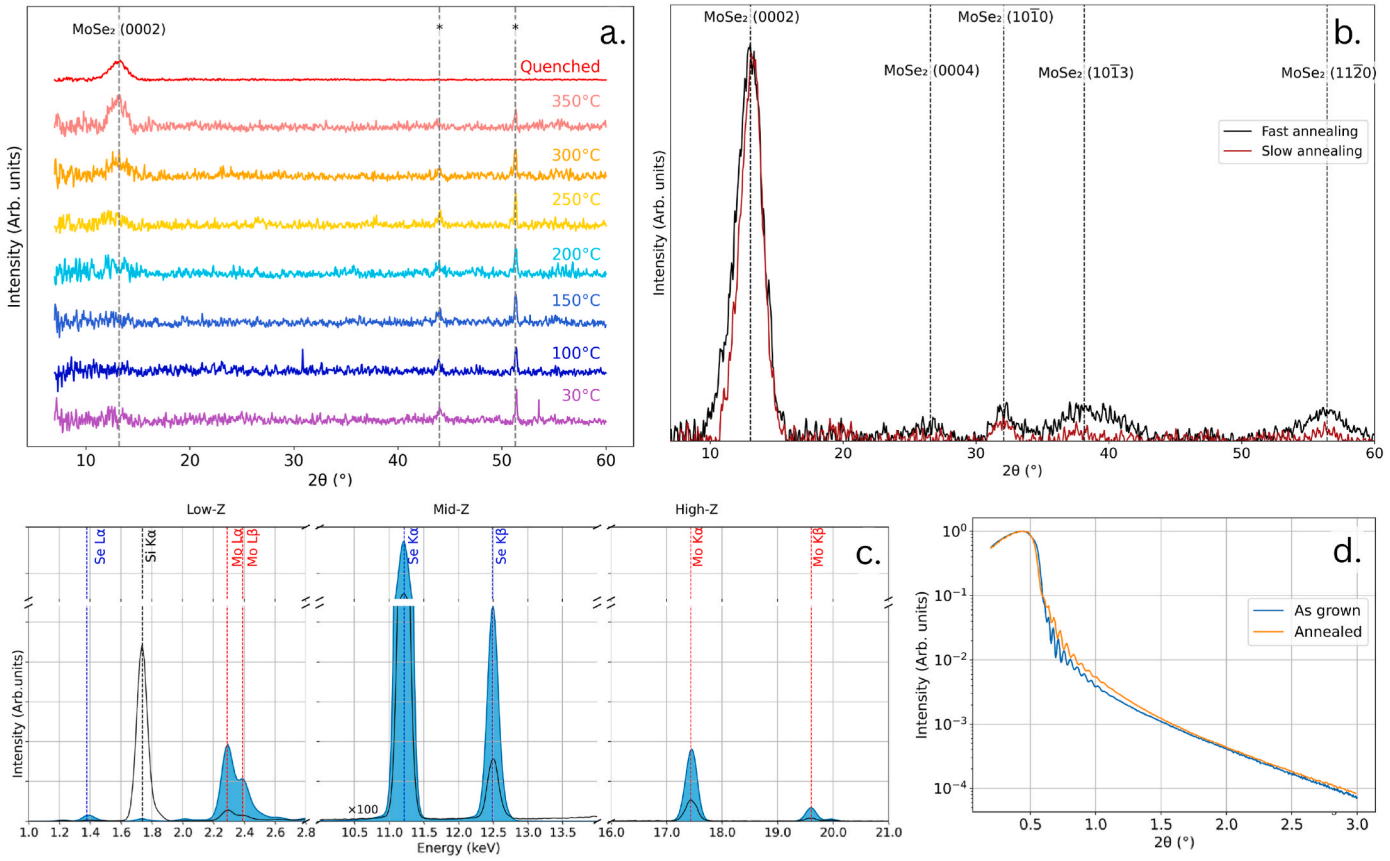

Fig. 1. *(a) X-ray GID (ω − 2θ) scans on MoSe2 sample annealed with slow treatment from 30 °C to 350 °C*
(b) Comparison of samples annealed with fast treatment (black) and step-by-step annealing (red), both presenting the same diffraction peaks.
(c)XRF spectra of $MoSe_2$ target (blue) and as deposited sample (black line).
(d)X-ray reflectivity (XRR) of a $MoSe_2$ sample before and after fast annealing. (For interpretation of the references to colour in this figure legend, the reader is referred to the Web version of this article.)

with the 2H phase and a a layered hexagonal crystal structure, where each molybdenum atom is sandwiched between two selenium atoms in a trigonal prismatic coordination, forming Se–Mo–Se layers stacked by weak van der Waals forces.

By repeating the annealing experiment with a different thermal treatment - heating the sample directly to 350 °C and cooling it down before collecting the spectrum during a 3-h measurement - we obtained the spectrum in Fig. 1b, (black curve labelled as 'fast annealing') where some additional peaks can be observed. All of the peaks were identified by fitting the experimental spectrum and assigned to $MoSe_2$ reflections. In particular, the peaks found at 13.02°, 26.55°, 32.09°, 38.05° and 56.43° were assigned to the (0002), (0004), (1010), (1013) and (1120) reflections, respectively [14]. This confirmed the formation of a preferred orientation (texture) in grains having their c-axis perpendicular to the substrate, corresponding to the (0002) peak. In addition, some degree of disorder was evidenced by the presence of prismatic plane reflections such as (1010) and (1120), while the observation of off-axis reflections like (1013) indicates tilted grains and polycrystallinity. The red curve in Fig. 1b, labelled as 'slow annealing', corresponds to a sample annealed by following the first annealing process described above, and the spectrum was obtained after cooling the sample down to RT. It was possible to identify the same diffraction peaks in both samples after the two different annealing processes. The peak assigned to the (0002) reflection, however, appears slightly shifted, being located at 13.02° in the "fast annealing" sample and at 13.15° in the "slow annealing" one. This angular shift corresponds to a variation of the lattice parameter $\Delta c = 0.014nm$. Although small, this difference reflects a relaxation of the lattice towards its bulk value (13.15°) in the slow-annealed sample, indicating a reduction of internal strain and improved crystalline quality compared to the fast-annealed one [15,16].

In conclusion, it turned out that the step-by-step annealing may promote the (000ℓ) orientation, but, in some cases, additional peaks are still observed, suggesting that other factors also play a significant role in determining the final crystalline orientation. To have a deeper insight into the structural feature of the MoSe2 film, we performed specular θ–2θ scans on our samples (not shown here). The obtained diffraction pattern shows the (0002) reflection of $MoSe_2$ together with the reflections of the Si substrate, while no additional $MoSe_2$ reflections are observed. This result is consistent with a polycrystalline film exhibiting a possible preferential alignment along the c-axis. Such preferential alignment is commonly reported for layered transition metal dichalcogenide thin films, where the van der Waals layered structure favors the growth of crystallites with their basal planes parallel to the substrate. We concluded that the absence of additional reflections in both the GIXRD and θ–2θ analysis is also consistent with limited crystallographic coherence and/or small grain size. As shown in Fig. 1c, the XRF spectra exhibit the characteristic emission lines of Se (blue) and Mo (red), consistent with the presence of both elements in the film. In particular, the intensity ratio between the Mo L_β and L_α lines is preserved ($L_\beta/L_\alpha \approx 0.54$ in both target and film), suggesting that the Mo spectral signature remains consistent after deposition. Small discrepancies in the K_β/K_α ratio are attributed to the lower signal-to-noise of the K_β line.

Despite the different scaling of the L and K lines, the Mo and Se peaks scale consistently relative to each other. Within the limitations of XRF, this is compatible with the nominal target composition. Accordingly, quantitative XRF analysis confirmed that the stoichiometry of the

deposited $MoSe_2$ film (Mo ≈ 33.8 at. %, Se ≈ 66.2 at.%) closely reproduces that of the sputtering target (Mo ≈ 33–35 at.%, Se ≈ 65–67 at. %), within ~5%.

To further investigate the structural modifications induced by the annealing process, X-ray Reflectivity (XRR) measurements were performed on both the as-deposited and annealed $MoSe_2/Si_3N_4$ films. The comparative XRR profiles are reported in Fig. 1d. It is worth noting thata both samples exhibit Kiessig fringes, indicating high morphological quality with smooth and parallel interfaces between the film and the substrate.

The XRR curves were analyzed using the Parratt formalism implemented in Bruker LEPTOS software, allowing extraction of film thickness and roughness parameters. The fitting yields a thickness of approximately 130 nm and a surface roughness of about 3 nm for the as-deposited film. After annealing, the thickness slightly decreases to approximately 125 nm, while the roughness increases to about 3.6 nm.

The increased roughness is consistent with the stronger damping of the Kiessig fringes observed in the annealed sample. These results indicate that annealing induces a slight reduction in thickness along with an increase in roughness. These XRR results, when considered together with the XRD data, support the conclusion that the annealed sample undergoes a transition to a crystalline state. This structural reorganization results in increased roughness at the nanoscale, a typical signature of polycrystalline growth. It has to be noted that some of the XRD spectra collected at RT prior to the annealing treatment showed the presence of the $MoSe_2$ (0002) diffraction peak. This observation was further investigated; after ruling out any correlation with growth parameters (such as chamber gas pressure and RF power), we found that achieving a fully amorphous film required performing a pre-sputtering step before each deposition run. This procedure was essential to minimize target surface contamination and stabilize the sputtering conditions.

Given the unexpected presence of the $MoSe_2$ (0002) diffraction peak in some as-deposited samples, and the structural modifications evidenced by XRR after the annealing, in particular the increased surface roughness, we further investigated the morphological evolution of the films by means of atomic force microscopy (AFM). This technique enables direct assessment of surface topography and nanoscale roughness, providing complementary insights to the XRR data and clarifying the effects of both the deposition process and thermal treatment on the structural properties of the films.

The AFM images (Fig. 2a and c) confirmed that the as-grown $MoSe_2$ films are continuous and fully cover the substrate, with no significant discontinuities in the scanned area. The apparent depressions observed in the AFM scans correspond to topographic height modulations between nanograins, rather than discontinuities in the MoSe2 layer. These

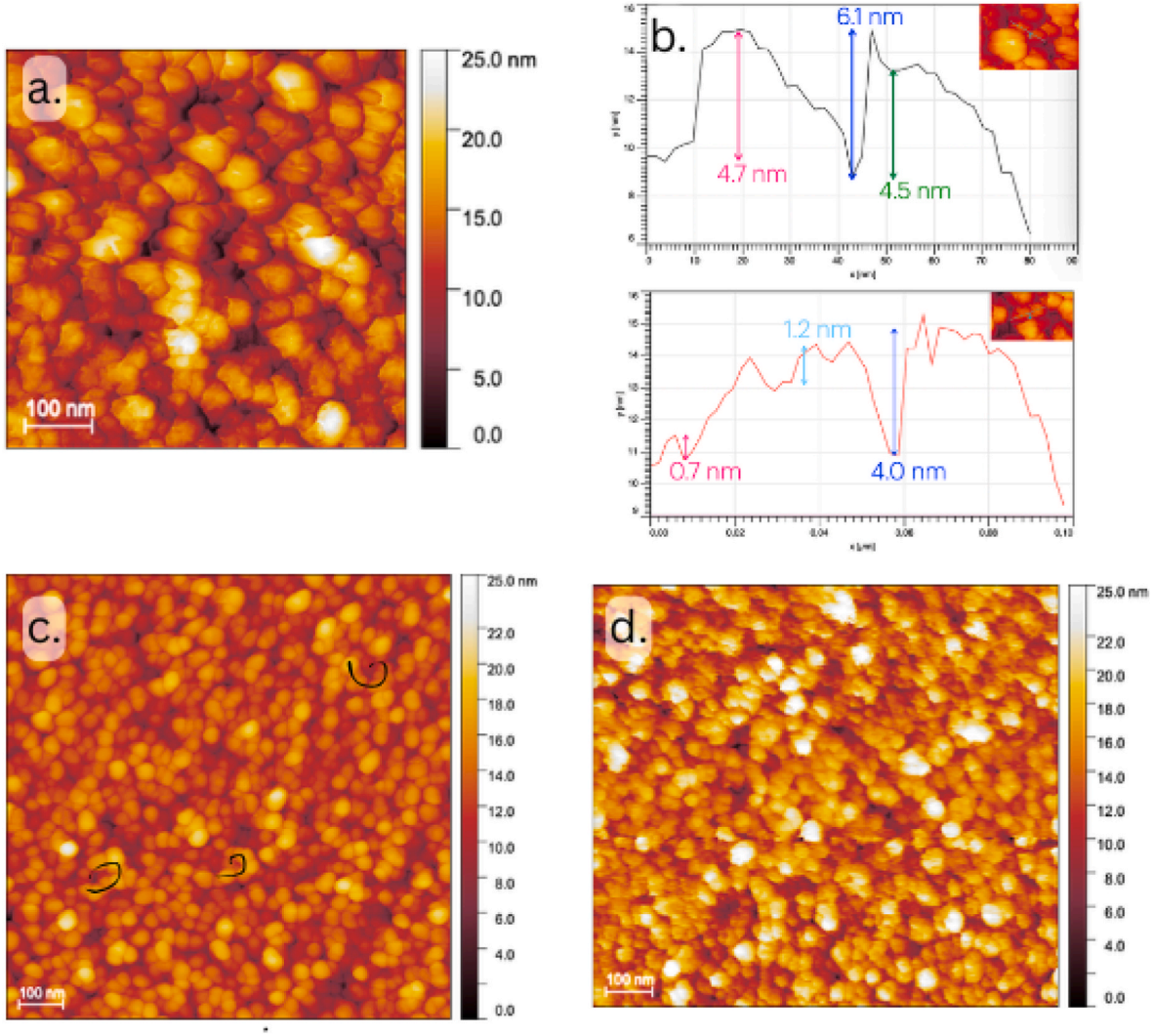

Fig. 2. Panel (a) displays the as grown sample, from which the line profiles shown in (b) were extracted to investigate surface roughness and morphological features. Panels (c) and (d) show AFM images of the as grown and crystalline samples, respectively. In panel (c) some spiral-like features are highlighted (black) for the reader's comprehension.

features are typical of the initial stages of grain formation in sputtered layered materials deposited at room temperature.

Spiral-like surface features can be observed in several regions of the film, highlighted with black

lines in panel (c), which are indicative of screw dislocation-driven growth mechanisms typically associated with layered materials [17, 18]. In our case, their presence in the as grown films (Fig. 2a and c) may indicate the onset of slight crystallization in the samples grown without pre-sputtering, in agreement with the structural characterization illustrated above. To further investigate this aspect, line profiles were extracted from selected regions to estimate the height differences between terraces and assess whether such features could be related to a layered structure. The extracted line profiles are shown in Fig. 2b, and they are consistent with the presence of terrace-like features with significant thickness variations across the film. In the as grown film, the surface exhibits prominent, rounded grains with radii on the order of several tens of nanometers. In the as grown sample, the topography is textured, with well-defined features and significant height modulations across the surface, as confirmed by the line profiles.

To assess the impact of annealing on surface morphology, AFM measurements were carried out on both as-deposited and annealed (crystalline) films.

Fig. 2c and d displays the AFM images of the two samples. The crystalline film in Fig. 2d shows densely packed nanograins and a generally smoother topographic appearance. Despite this, a slight increase in RMS roughness is observed following the crystallization process, with values of 3.4 nm for the as grown film and 3.6 nm for the crystalline one. This suggests that crystallization induces surface reorganization, possibly associated with grain rearrangement and localized vertical growth.

To further quantify the morphological evolution, grain size analysis was performed on the AFM images. Grains were identified through watershed-based segmentation, and their equivalent radii were extracted to construct size distributions, which were normalized to account for differences in density. The grain size distributions highlight the distinction between the two samples. The as grown film exhibits a broad distribution, with a most frequent grain radius of approximately 7 nm and a significant tail toward larger grain sizes, consistent with a less uniform morphology. In contrast, the crystalline film displays a narrower distribution centered around 10 nm, reflecting increased uniformity and higher density, with limited grain coarsening. These results indicate that the thermal annealing promotes both grain growth and a more homogeneous grain structure. Such morphological transformations are expected to play a crucial role in determining the functional properties of the $MoSe_2$ films, particularly in terms of their electronic and optical behavior, which are highly sensitive to surface roughness, grain size distribution, and overall crystallinity. Despite the apparent grain growth, the increase in lateral size remains modest, suggesting limited coarsening during the amorphous-to-crystalline transition.

In addition to this analysis, a secondary segmentation was performed using a lower height threshold, aimed at identifying and quantifying depressions or unfilled regions between grains. This analysis revealed that, upon crystallization, the number of unfilled regions decreases and their average size shrinks, pointing to improved film compactness and reduced surface porosity. Additionally, a slight increase in the overall z-scale (perpendicular to the sample surface) was observed after annealing, consistent with the formation of vertical crystalline domains and localized out-of-plane growth. Taken together, these findings demonstrate that the thermal annealing not only enhances grain ordering and size uniformity, but also reduces void density and promotes vertical growth. Such morphological transformations are crucial for tuning the electrical and optical performances of $MoSe_2$ thin films, particularly in heterostructure-based devices where interface quality and film continuity are critical.

To complement the morphological analysis and further investigate the short-range structural order of the films, Raman spectroscopy was performed on both as-grown and annealed (crystalline) $MoSe_2$ samples (130 nm), as shown in Fig. 3a. While AFM provides direct insight into the surface topography and grain distribution, Raman spectroscopy probes the local vibrational properties and bonding environment, enabling the identification of short-range structural changes. The combined use of both techniques provides a comprehensive picture of the film's evolution upon thermal treatment. As shown in Fig. 3a, the Raman spectrum of the as grown film (blue) exhibits a peak attributable to the substrate, along with a feature around 250 cm^{-1} that probably can be ascribed to the unresolved A_1g and E_2g modes. This suggests a significant degree of short-range structural order and the formation of characteristic $MoSe_2$ local bonding units already during the sputtering process at room temperature. Following thermal annealing, as displayed in Fig. 3a (orange), Raman-active modes of few-layer $MoSe_2$ were clearly observed, including the E_1g (~169 cm^{-1}), A_1g (~242 cm^{-1}), and E_2g^1 (~287 cm^{-1}) modes, all compatible with literature values reported for the 2H phase of $MoSe_2$ [19]. The observation of these modes indicates trigonal prismatic coordination of Mo by Se, consistent with the local structural motifs of layered $MoSe_2$. In addition to the expected features of the 2H phase, three additional peaks are observed in the crystalline sample, located at approximately 148 cm^{-1} (labelled with *), 442 cm^{-1} (labelled with **), and 582 cm^{-1} (labelled with ***). These peaks are not predicted by the group theory for the ideal 2H structure and do not correspond to known fundamental phonon modes.

Their presence suggests the activation of otherwise forbidden vibrational processes, often attributed to local symmetry breaking, disorder, or multi-phonon scattering. The low-frequency peak at 148 cm^{-1} (*) lies close to the longitudinal acoustic mode at the M point (LA(M)) and is likely associated with it [15]. Its activation is commonly interpreted as a signature of structural disorder or finite-size effects that relax the Raman selection rules [20].

The spectrum feature at 442 cm^{-1} (**) does not correspond to any single-phonon vibration, but falls within the spectral region of known two-phonon combinations involving acoustic and optical modes [20]. Similarly, the peak at 582 cm^{-1} (***) is compatible with higher-order phonon processes. According to the resonance Raman study by Soubelet et al. [20], these features can be attributed to combinations such as $E'(M) + LA(M)$ and $E'(M) + 2LA(M)$, which emerge under resonant excitation. In particular, (**) matches well with the $E'(M) + 2LA(M)$ process, while (***) can be associated with either LA(M) overtones or mixed acoustic–optical combinations. The presence of these peaks supports the interpretation of a structurally disordered material in which symmetry breaking allows the activation of multi-phonon processes. Following thermal annealing, the Raman spectrum exhibits a general sharpening of the main phonon modes, consistent with the formation of textured crystalline grains. However, the persistence of the additional peaks in the crystalline state indicates that local disorder and resonance-enhanced phonon interactions remain relevant even after the transition to a more ordered phase. This observation is compatible with the presence in GID spectra of prismatic planes and off-axis reflections.

Overall, the Raman results, together with the XRD data, indicated an increase in crystallinity of the films after annealing. Additionally, the observation of both fundamental and combination modes provides further insight into the complexity of vibrational behavior in $MoSe_2$ thin films and reinforces the impact of thermal treatment on their microstructural properties. Given that the vibrational spectra reflect a disordered or partially ordered structure, we proceeded to investigate whether such structural characteristics also impact the electrical behavior of the films. To this end, four-point probe measurements were carried out to evaluate the resistivity of the $MoSe_2$ film. To characterize the transport properties of the $MoSe_2$ films, we performed resistance measurements using a four-point probe configuration on two sets of samples, with thicknesses of 20 nm and 80 nm, deposited on quartz substrates. Notably, these samples were grown in the same deposition runs as those on Si (100) substrates used for the other characterizations,

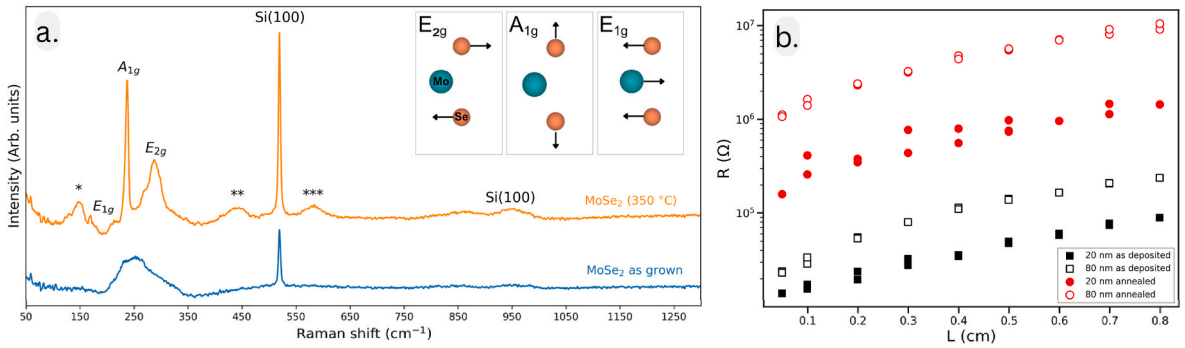

Fig. 3. (a) Raman measurements on a MoSe2 single layer at RT as grown (blue) and after annealing at 350 C. The inset shows a scheme of the main MoSe2 vibrational modes E1g, E2g, A1g.
(b) Resistance, normalized to a thickness of 100 nm, as a function of probe spacing. Square markers correspond to as-grown samples, while circular markers represent annealed samples; filled and open symbols distinguish the 20 nm and 80 nm films, respectively. (For interpretation of the references to colour in this figure legend, the reader is referred to the Web version of this article.)

ensuring material consistency across all measurements. For both thicknesses, measurements were collected in the as-grown state and after thermal annealing (crystalline phase). Preliminary I-V characterizations confirmed the formation of ohmic contacts in all configurations, ensuring that the measured resistance values reflect the intrinsic bulk properties of the material.

The analysis of the resistance dependence on probe spacing (Fig. 3b) reveals a consistent behavior across both film thicknesses. In the as-grown state, the experimental data display a clear linear trend with increasing length, indicating homogeneous conductivity throughout the as-grown matrix. Specifically, for the 20 nm film, the calculated resistivity is $\rho \approx 8.6 \times 10^{-1}$ Ω cm, while the 80 nm as-grown sample shows a resistivity of $\rho \approx 2.2$ Ω cm. Upon thermal annealing, the transition to the crystalline phase—confirmed by the appearance of characteristic peaks in the XRD spectra—leads to a significant modification of the transport properties. For both film thicknesses, the resistivity increases markedly when transitioning to the crystalline phase, reaching values of $\rho \approx 1.5 \times 10^{-1}$ Ω cm and $\rho \approx 9.3 \times 10^{1}$ Ω cm for the 20 nm and 80 nm samples, respectively. The electrical measurements reveal a counterintuitive increase in resistivity upon annealing, despite AFM evidence of improved grain uniformity. This behavior is not unprecedented. In particular, Bichsel and Lévy [21] have reported that MoSe2 films grown at low substrate temperatures exhibit relatively low resistivity in the as-deposited state, but, after annealing, their RT resistivity increases by more than one order of magnitude. They have attributed this effect to the development of a lamellar microstructure with reduced interconnection between crystallites. Similarly, Mallouky and Bernède [16] have investigated $MoSe_2$ thin films obtained by a solid-state reaction and have reported room-temperature resistivity values for crystalline/as-grown films ranging from 0.1×10^3 to 15×10^3 Ω cm. They have found that the resistivity increases as the grain size decreases and/or the crystallite order deteriorates, emphasizing the strong influence of film morphology on charge transport. A comparable behavior has also been observed for MoS_2 thin films [22], suggesting that this mechanism is a general feature of layered TMDs.

Building upon the structural characterization of $MoSe_2$ films, we extended our investigation to a vertically stacked heterostructure that combines $MoSe_2$ as TMDC layer material and $Ge_2Sb_2Te_5$ (GST225) as active PCM memory material in a controlled multilayer geometry. The heterostructure under investigation consists of a multilayer stack designed to study the structural and thermal behavior of phase-change and TMD materials in close contact. The structure is composed of two repetitions, each consisting of 20 nm of GST225, 5 nm of $MoSe_2$, and another 20 nm of GST225, all deposited on a Si(100) substrate. The specific layer thicknesses within the heterostructure were selected to balance technological growth limits with device performance. Physically, the 5 nm thickness represents the lower limit to ensure a continuous, uniform, and closed $MoSe_2$ potential confinement barrier over the underlying GST, preventing discontinuities during room-temperature RF sputtering. From an electrical perspective, while the 20 nm GST layers provide sufficient active volume to preserve a high and detectable resistance contrast, the highly resistive $MoSe_2$ interlayer must be kept ultrathin. This minimizes parasitic resistance, preventing an unwanted increase in the device's programming voltage. Notably, the GST225 layer used in this study was deposited using sputtering conditions specifically optimized to delay full trigonalization at 300 °C. To provide further insight into the layered structure, we would need additional investigation such as Time-of-Flight Secondary Ion Mass Spectrometry (ToF-SIMS) to obtain a depth profile exhibiting a modulated intensity as a function of the sputtering time, evidencing the presence of periodically alternated $MoSe_2$ and GST layers in the structure. Furthermore, additional local area structural analysis such as cross-sectional TEM would be required for a complete structural analysis. Although the trigonal phase of GST is typically favored at higher annealing temperatures [22], here we deliberately selected a more stable, slightly under-crystallized GST, to reduce surface corrugation and prevent excessive undulations in the stacked heterostructure. As discussed by Raoux et al. [1], the trigonal phase of GST is associated with increased atomic ordering and denser packing, which can induce surface roughening during growth or annealing. By maintaining a largely cubic or partially as-grown phase at 300 °C, we aimed to preserve a flatter interface and minimize strain propagation into the $MoSe_2$ layer. To probe the evolution of the structural phases, GID measurements were performed at various temperatures, from 30 °C up to 300 °C, as well as after quenching the sample and repeating the measurement at RT. After evaluating the effect of the two different annealing procedures described above, we selected the slower thermal ramp to ensure the formation of a more ordered crystalline $MoSe_2$ phase within the heterostructure. The resulting diffraction patterns reveal distinct peaks corresponding to both the cubic and trigonal phases of GST (all reflections labelled in Fig. 4a), as well as a peak attributed to the $MoSe_2$ (0002) reflection. The data show the progressive crystallization of GST upon heating, with well-defined reflections emerging above 150 °C. Observing the XRD spectra, we noted that, as expected, GST225 does not undergo a complete phase transition even at 300 °C. This behavior is consistent with the sputtering conditions adopted during the deposition. Specifically, the GST225 layer was grown at a lower pressure than that commonly used in standard recipes.

It has been reported that higher sputtering pressures lead to lower phase transition temperatures, due to increased disorder and internal stress accumulation during growth [22]. Films grown at lower pressure are typically denser and more homogeneous, as the increased kinetic energy of incident species promotes compact atomic packing and reduces porosity [23]. In such tightly packed configurations, the

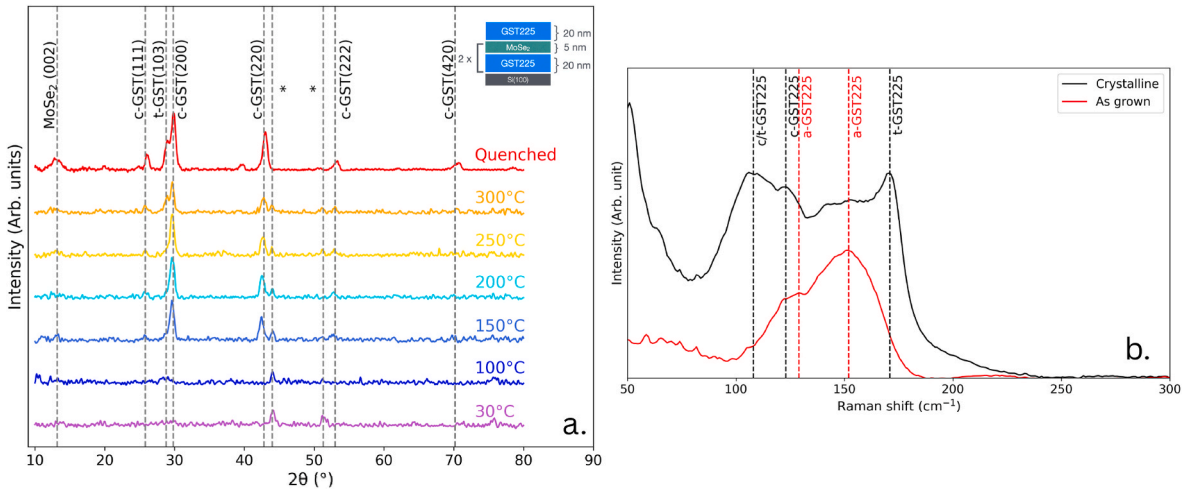

Fig. 4. (a) X-ray GID ($\omega - 2\theta$) scans at different temperatures and after annealing. The measurements refer to the multilayer heterostructure illustrated schematically in the inset. XRD peaks show the coexistence after annealing of both cubic and trigonal phase of GST225 as well as the $MoSe_2$ (0002) reflection.
(b) Raman spectra of as grown (red) and crystalline (black) GST225/$MoSe_2$ heterostructure. (For interpretation of the references to colour in this figure legend, the reader is referred to the Web version of this article.)

activation energy for crystallization is higher and the transition to the trigonal phase requires higher thermal input. Additionally, stress-induced nucleation, which often facilitates crystallization at lower temperatures in defective or porous films [1] is minimized. This combination of higher structural cohesion and reduced defect-driven nucleation pathways results in partial retention of the cubic GST phases even after annealing at 300 °C.

To further investigate the structural evolution, Raman spectroscopy was performed before and after annealing up to 300 °C on a heterostructure similar in composition to the one analyzed by XRD but differing in layer configuration. This sample consists of four repetitions of alternating GST225 (20 nm)/$MoSe_2$ (5 nm) bilayers, capped by a topmost GST225 (20 nm) layer. The corresponding Raman spectra are shown in Fig. 4b for the as-grown (red) and annealed (black) sample. The coexistence of the two crystalline phases of GST225 is confirmed by the identification of distinct vibrational modes: the band at 123 cm^{-1} is consistent with the cubic phase, while the peak at 172 cm^{-1} indicates the emergence of the trigonal phase upon annealing, in agreement with literature values [15].

No Raman features attributable to $MoSe_2$ are observed. This absence is consistent with the optical geometry of the stack. At 532 nm excitation, cubic GST exhibits a short absorption depth ($\delta \approx 13$ nm), so that the first 20 nm GST already reduces the excitation reaching the underlying $MoSe_2$ to ~22%, and the corresponding Raman scattering signal must cross the same GST layer again on the way out. A simple Beer–Lambert attenuation estimate indicates that the Raman contribution of the top GST layer is about 30 times larger than that of the first $MoSe_2$ layer, while deeper $MoSe_2$ layers are even more strongly suppressed. As a result, the Raman spectrum is dominated by GST modes, and $MoSe_2$ vibrations remain undetectable.

To position the proposed MoSe2/GST225 heterostructure within the state of the art, a targeted comparison with select reference studies on TMD-based interlayers is summarized in Table 1. While advanced telluride interlayers, such as TiTe2 and HfTe2, offer excellent lattice matching [8,24,25] they often exhibit limited thermal budgets that trigger elemental interdiffusion during high-temperature processing. Overall, this baseline comparison shows that different TMDs have been explored for PCM heterostructures, each offering specific advantages depending on the intended application; in this context, our approach provides a promising trade-off. The utilization of room-temperature RF sputtering avoids any high-thermal-budget steps, ensuring full back-end-of-line industrial compatibility.

Table 1
Comparative analysis of different transition metal chalcogenide interlayers in phase-change memory (PCM) heterostructures: deposition methods, thermal budget, and performance trade-offs.

Interlayer/ Heterostructure Thermal Stability Limit	Deposition Method	Enhanced Features	Open Challenges	Reference
$TiTe_2$/Sb-based PCM 250 °C	Sputtering (often requiring substrate heating)	Outstanding lattice matching, exceptionally low resistance drift.	Prone to minor Te interdiffusion at higher thermal budgets.	Kim et al. (Small, 2024) [24]
$HfTe_2/Sb_2Te_3$ 250-280 °C	Chemical/ Physical Vapor Deposition	High crystalline quality, sharp initial interfaces.	Restricted thermal budget, high susceptibility to ambient oxidation.	Park et al. (JMST, 2025) [25]
MoS_2/GST 350 °C	HighTemp.- CVD/ Sputtering	Excellent mechanical robustness and local thermal isolation.	Sulfides exhibit high chemical mismatch and high interface state density.	Ning et al. (ACS AMI, 2022) [8]
$MoSe_2$/ $Ge_2Sb_2Te_3$ 300 °C	Room Temp.- RF Sputtering	Industry-compatible low thermal budget, potential diffusion barrier up to 300 °C, improved electro-thermal confinement.	Resistivity increase upon annealing requires ultra-thin layer optimization (≤5 nm).	This Work

In this work, we investigated the structural, morphological, vibrational, and electrical evolution of sputtered $MoSe_2$ thin films and their integration into GST225-based heterostructures. As-deposited $MoSe_2$ films are crystallize into the a structure compatible with the 2H hexagonal structure upon annealing above 250 °C, developing in some cases preferential (000ℓ) orientation and increased density. AFM and XRR revealed that crystallization leads to a reorganization into compact nanograins, accompanied by a modest increase in roughness and

improved film compactness. Raman spectroscopy confirmed the onset of crystallinity, while also highlighting the presence of disorder-related features. Electrical measurements highlighted a counterintuitive increase in resistivity after crystallization, pointing to the critical role of film morphology and grain connectivity in charge transport. When integrated into GST225/$MoSe_2$ heterostructures, the $MoSe_2$ films preserve stoichiometry and structural integrity under annealing up to 300 °C. Although the Raman response of $MoSe_2$ films was strongly suppressed by the limited optical penetration depth of GST, XRD confirmed their crystalline stability within the stack. These results demonstrated that sputtered $MoSe_2$ combines chemical robustness, thermal stability, and structural compatibility with GST225, establishing it as a promising candidate as interlayer material for next-generation phase-change memories. he results show that sputtered $MoSe_2$ remains structurally stable after annealing and is compatible with GST225. Although this work does not address device performance, it provides the experimental basis needed before investigating the role of $MoSe_2$ interlayers in complete PCM devices.

The results show that sputtered $MoSe_2$ remains structurally stable after annealing and is compatible with GST225. Although this work does not address device performance, it provides the experimental basis needed before investigating the role of $MoSe_2$ interlayers in complete PCM devices.

3. Experimental methods

3.1. Samples growth

The $MoSe_2$ thin films were deposited by RF-sputtering in a custom-made high vacuum chamber system (IONVAC PROCESS srl, Pomezia, Italy), equipped with a planetary system for deposition and four confocal targets. The heterostructures were grown at RT on Si(100) substrates (p-type, $\rho = 1 \div 10\ \Omega$cm) with a thin native oxide layer on top. The $MoSe_2$ targets were provided by Robeko GmbH & Co. KG (Mehlingen, Germany), with a 99.99% purity. The chamber pressure was kept at 6.5×10-3 mbar.

Standard pre-sputtering was performed for 5 min at working power with the target shutter closed, prior to growth from the $MoSe_2$ and Si_3N_4 targets.

The sputtering forward power was 30 W or 50 W, and a flow 5.86 SCCM of pure argon was sent to the growth chamber. The GST growth rate was monitored with an STM-2 rate monitor (INFICON Holding AG, Bad Ragaz, Switzerland).

3.2. X-ray fluorescence (XRF)

Energy dispersive X-ray Fluorescence (XRF) measurements were performed ex-situ using a RIGAKU Nex DE VS spectrometer (APPLIED RIGAKU TECHNOLOGIES INC., Austin, Texas, USA) equipped with a 60 kV X-ray tube and a silicon drift detector.

3.3. X-ray diffraction (XRD)

XRD measurements were performed ex-situ by a D8 Discover diffractometer (BRUKER, Billerica, Massachusetts, USA) equipped with a Cu X-ray source (Cu-Kα1 radiation $\lambda = 1.54$ Å, 40 kV and 40 mA) and a DHS1100 dome-type heating stage (ANTON PAAR, Graz, Austria) for temperature measurements in N_2 atmosphere. Grazing incidence diffraction (GID) (ω - 2θ) scans were acquired at different temperatures (T = 30 – 350 °C) during sample annealing.

3.4. Raman

Raman spectra were acquired ex situ by means of a DXR2xi Raman imaging microscope (Thermo Fischer, Waltham, Massachusetts, USA) equipped with a 532 nm laser source and a 50x objective. The Raman data acquisition was performed at RT in back-scattering geometry, using a 4 mW laser power at the sample surface.

3.5. Atomic force microscopy

The surface morphology of the $MoSe_2$ films was examined ex situ with a Veeco Multimode Nanoscope IIIa atomic force microscope operating in tapping mode under ambient conditions. Height maps were collected over scan areas ranging from $0.6 \times 0.6\ \mu m^2$ to $5 \times 5\ \mu m^2$. Raw images were flattened to remove background tilt, and roughness and grain size statistics were extracted via watershed-based segmentation in Gwyddion.

3.6. Electrical measurements

The R-L characteristics were measured in air in a probe station equipped with sourcemeters (KEITHLEY 2470 and 236, TEKTRONIX INC.). The four-point collinear probe technique was used to calculate the resistivity as $\rho = \pi/\ln 2 \times R \times t \times R1$, where R is the resistance, t is the film thickness and R1 is the Haldor Topsøe correction factor for thin samples of finite rectangular shape [19].

CRediT authorship contribution statement

Agnese Foglietti: Writing – review & editing, Writing – original draft, Methodology, Investigation, Data curation, Conceptualization. **Sara De Simone:** Writing – review & editing, Writing – original draft, Methodology, Investigation, Data curation, Conceptualization. **Adriano Diaz Fattorini:** Investigation. **Sabrina Calvi:** Investigation, Data curation. **Valentina Mussi:** Writing – review & editing, Investigation. **Christian Petrucci:** Investigation. **Fabrizio Arciprete:** Writing – review & editing, Writing – original draft, Resources, Investigation. **Massimo Longo:** Writing – review & editing, Writing – original draft, Resources, Methodology, Funding acquisition, Conceptualization. **Raffaella Calarco:** Writing – review & editing, Writing – original draft, Resources, Methodology, Investigation, Funding acquisition, Data curation, Conceptualization.

Declaration of competing interest

The authors declare the following financial interests/personal relationships which may be considered as potential competing interests: Sara De Simone, Raffaella Calarco, Massimo Longo reports administrative support was provided by Italian Ministry of University and Research (MUR) through project PRIN2020 Emphasis CUP B87G20000160001. Agnese Foglietti reports was provided by Department of Chemical Science and Technology, Univerity of Tor Vergata. Fabrizio Arciprete, Adriano Diaz Fattorini reports was provided by National Recovery and Resilience Plan (NRRP), Mission 4 Component 2 Investment 1.5 (D.M 351,2022). If there are other authors, they declare that they have no known competing financial interests or personal relationships that could have appeared to influence the work reported in this paper.

Acknowledgements

This work was supported by the Italian Ministry of University and Research (MUR) through project PRIN2020 Emphasis CUP B87G20000160001, the XL doctoral program in Chemical Sciences, Department of Chemical Science and Technology, University of Rome Tor Vergata, with financial support from PNRR Mission 4, Component 2 “Dalla ricerca all'impresa” – Investment 3.3 (A.F.), National Recovery and Resilience Plan (NRRP), Mission 4 Component 2 Investment 1.5 (D. M 351,2022) (F.A., A.D.F.). M.L. acknowledges the Grant MUR Dipartimento di Eccellenza 2023−27 X-CHEM project.

Data availability

The data that supports the findings of this study are available from the corresponding author upon reasonable request.

References

[1] S. Raoux, Phase change materials, Annu. Rev. Mater. Res. 39 (1) (Aug. 2009) 25–48, https://doi.org/10.1146/annurev-matsci-082908-145405.

[2] H.-S.P. Wong, et al., Phase change memory, Proc. IEEE 98 (12) (Dec. 2010) 2201–2227, https://doi.org/10.1109/JPROC.2010.2070050.

[3] M. Bertelli, et al., Stable chalcogenide Ge–Sb–Te heterostructures with minimal Ge segregation, Sci. Rep. 14 (1) (Jul. 2024) 15713, https://doi.org/10.1038/s41598-024-66441-y.

[4] W. Yang, N. Hur, D.-H. Lim, H. Jeong, J. Suh, Heterogeneously structured phase-change materials and memory, J. Appl. Phys. 129 (5) (Feb. 2021), https://doi.org/10.1063/5.0031947.

[5] (PDF) phase-change Heterostructure Enables Ultralow Noise and Drift for Memory Operation," ResearchGate, doi: 10.1126/science.aay0291.

[6] Y. Chen, et al., Emerging horizons in phase-change materials for non-volatile memory, Mater. Today Adv. 25 (Mar. 2025) 100571, https://doi.org/10.1016/j.mtadv.2025.100571.

[7] T.H. Kim, S.W. Park, H.J. Lee, D.H. Kim, J.Y. Choi, T.G. Kim, Effect of transition metal dichalcogenide based confinement layers on the performance of phase-change heterostructure memory, Small 19 (48) (2023) 2303659, https://doi.org/10.1002/smll.202303659.

[8] J. Ning, et al., Low energy switching of phase change materials using a 2D thermal boundary layer, ACS Appl. Mater. Interfaces 14 (36) (Sep. 2022) 41225–41234, https://doi.org/10.1021/acsami.2c12936.

[9] J.-J. Ma, J.-J. Zheng, W.-D. Li, D.-H. Wang, B.-T. Wang, Thermal transport properties of monolayer $MoSe_2$ with defects, Phys. Chem. Chem. Phys. 22 (10) (2020) 5832–5838, https://doi.org/10.1039/d0cp00047g.

[10] W. Choi, N. Choudhary, G.H. Han, J. Park, D. Akinwande, Y.H. Lee, Recent development of two-dimensional transition metal dichalcogenides and their applications, Mater. Today 20 (3) (Apr. 2017) 116–130, https://doi.org/10.1016/j.mattod.2016.10.002.

[11] J. Pouzet, J.C. Bernede, MoSe2 thin films synthesized by solid state reactions between Mo and Se thin films, Rev. Phys. Appl. 25 (8) (1990) 807–815, https://doi.org/10.1051/rphysap:01990002508080700.

[12] W. Zhan, J. Zou, X. Mao, L. Tang, H. Wei, Structure and tribological properties of MoSe2 films prepared by two-step process, Trans. Nonferrous Met. Soc. China 33 (8) (Aug. 2023) 2483–2496, https://doi.org/10.1016/S1003-6326(23)66275-2.

[13] Z. Dehghani, F. Ostovari, M. Nadafan, Investigation of the structural, dielectric, and optical properties of MoSe2 nanosheets, J. Appl. Phys. 131 (21) (Jun. 2022) 213101, https://doi.org/10.1063/5.0088016.

[14] W. Li, et al., Molybdenum diselenide – black phosphorus heterostructures for electrocatalytic hydrogen evolution, Appl. Surf. Sci. 467 (468) (Feb. 2019) 328–334, https://doi.org/10.1016/j.apsusc.2018.10.127.

[15] S. Santhosh, R. Rajasekar, V.K. Gobinath, C. Moganapriya, S. Arun Kumar, A. Manju Sri, Influence of electrosprayed MoSe2 antireflective surface coatings on performance of multicrystalline silicon solar cell, Silicon 14 (11) (Jul. 2022) 6039–6051, https://doi.org/10.1007/s12633-021-01385-w.

[16] A. Mallouky, J.C. Bernede, Characterization of MoSe2 thin films, Thin Solid Films 158 (2) (Apr. 1988) 285–298, https://doi.org/10.1016/0040-6090(88)90032-6.

[17] X. Wang, et al., Weakened interlayer coupling in two-dimensional MoSe2 flakes with screw dislocations, Nano Res. 12 (8) (Aug. 2019) 1900–1905, https://doi.org/10.1007/s12274-019-2456-y.

[18] L. Zhang, et al., Three-dimensional spirals of atomic layered MoS_2, Nano Lett. 14 (11) (Nov. 2014) 6418–6423, https://doi.org/10.1021/nl502961e.

[19] D. Nam, J.-U. Lee, H. Cheong, Excitation energy dependent raman spectrum of MoSe2, Sci. Rep. 5 (1) (Nov. 2015) 17113, https://doi.org/10.1038/srep17113.

[20] P. Soubelet, A.E. Bruchhausen, A. Fainstein, K. Nogajewski, C. Faugeras, Resonance effects in the Raman scattering of monolayer and few-layer MoSe 2, Phys. Rev. B 93 (15) (Apr. 2016) 155407, https://doi.org/10.1103/PhysRevB.93.155407.

[21] R. Bichsel, F. Lévy, Electrical and optical properties of MoSe2 films prepared by r.f. magnetron sputtering, Thin Solid Films 124 (1) (Feb. 1985) 75–83, https://doi.org/10.1016/0040-6090(85)90031-8.

[22] M. Krbal, J. Prikryl, I. Pis, V. Prokop, J. Rodriguez Pereira, A.V. Kolobov, Anomalous electrical conductivity change in MoS2 during the transition from the amorphous to crystalline phase, Ceram. Int. 49 (2) (Jan. 2023) 2619–2625, https://doi.org/10.1016/j.ceramint.2022.09.242.

[23] S. Calvi, et al., Ge enrichment of ge–sb–te alloys as keystone of flexible edge electronics, Adv. Electron. Mater. 11 (2) (2025) 2400184, https://doi.org/10.1002/aelm.202400184.

[24] D.H. Kim, et al., Phase change heterostructure memory with oxygen-doped Sb_2Te_3 layers for improved durability and reliability through nano crystalline Island formation, Small 20 (34) (Aug. 2024) 2312249, https://doi.org/10.1002/smll.202312249.

[25] S.W. Park, et al., Phase-change heterostructure with HfTe2 confinement sublayers for enhanced thermal efficiency and low-power operation through Joule heating localization, J. Mater. Sci. Technol. 204 (Jan. 2025) 104–114, https://doi.org/10.1016/j.jmst.2024.02.072.